

Optimal Heliocentric transfers of a Sun-facing Heliogyro

Marco Bassetto, Alessandro A. Quarta*, Andrea Caruso, Giovanni Mengali

Dipartimento di Ingegneria Civile e Industriale, University of Pisa, Italy

Abstract

A heliogyro is a rotating solar sail with the reflecting surface divided into a number of long and slender blades, which are stiffened by a spin-induced centrifugal force. Each blade can rotate around its own longitudinal axis so as to change the pitch angle and allow the thrust vector to be effectively controlled. The aim of this paper is to analyze the optimal heliocentric transfers of a Sun-facing heliogyro, that is, a heliogyro whose fundamental plane is always perpendicular to the Sun-spacecraft line. A simplified analytical model of the thrust and torque vectors provided by a Sun-facing heliogyro is illustrated, using the characteristic acceleration as a performance parameter. The proposed thrust vector model is then exploited to calculate the minimum flight times in a set of two-dimensional heliocentric transfers. Using an indirect method and a semi-analytical approach for trajectory optimization, some exemplary cases are discussed, such as circle-to-circle Earth-Mars and Earth-Venus transfers or a simplified mission to the asteroid 25143 Itokawa.

Keywords: heliogyro, spinning solar sail, trajectory optimization, heliocentric orbit transfer

Nomenclature

A_{tot}	=	total reflective area, [m ²]
a	=	semimajor axis, [au]
\mathbf{a}	=	propulsive acceleration vector, [mm/s ²]
a_c	=	characteristic acceleration, [mm/s ²]
a_p	=	component of \mathbf{a} along $\hat{\mathbf{p}}$, [mm/s ²]
a_r	=	component of \mathbf{a} along $\hat{\mathbf{r}}$, [mm/s ²]
a_t	=	component of \mathbf{a} along $\hat{\mathbf{t}}$, [mm/s ²]
C	=	heliogyro center of mass
C_k	=	k -th blade center of mass
$\hat{\mathbf{d}}$	=	unit vector
e	=	orbital eccentricity
\mathbf{F}_k	=	radiation pressure force on the k -th blade, [N]
i	=	orbital inclination, [rad]
$\{\hat{\mathbf{i}}, \hat{\mathbf{j}}, \hat{\mathbf{k}}\}$	=	unit vectors of \mathcal{T}_B
$\{\hat{\mathbf{i}}_k, \hat{\mathbf{j}}_k, \hat{\mathbf{k}}_k\}$	=	unit vectors of \mathcal{T}_k
\mathcal{J}	=	cost function
l	=	blade length, [m]
\mathbf{M}	=	total torque vector, [N m]
m	=	total spacecraft mass, [kg]
N	=	number of blades

*Corresponding author

Email addresses: marco.bassetto@ing.unipi.it (Marco Bassetto), a.quarta@ing.unipi.it (Alessandro A. Quarta), andrea.caruso@ing.unipi.it (Andrea Caruso), g.mengali@ing.unipi.it (Giovanni Mengali)

O	= Sun's center of mass
P	= solar radiation pressure, [Pa]
p	= osculating orbit semilatus rectum, [au]
$\{\hat{\boldsymbol{p}}, \hat{\boldsymbol{t}}\}$	= normal and transverse unit vectors
r	= Sun-spacecraft distance, [au]
$\hat{\boldsymbol{r}}$	= radial unit vector
S	= spacecraft center of mass
T	= orbital period, [days]
t	= time, [days]
\mathcal{T}_B	= spacecraft-fixed (body) reference frame
\mathcal{T}_k	= blade-fixed reference frame
\mathcal{T}_\odot	= heliocentric polar reference frame
\boldsymbol{v}	= spacecraft inertial velocity vector, [km/s]
v_r	= radial component of \boldsymbol{v} , [km/s]
v_t	= transverse component of \boldsymbol{v} , [km/s]
w	= blade width, [m]
α	= thrust angle, [rad]
α_d	= angle between $\hat{\boldsymbol{d}}$ and $\hat{\boldsymbol{r}}$, [rad]
α_n	= cone angle, [rad]
γ	= auxiliary angle, [rad]
δ_n	= clock angle, [rad]
ζ_k	= angular position of the k -th blade, [rad]
ϑ	= control parameter, [rad]
θ_k	= pitch angle of the k -th blade, [rad]
μ_\odot	= Sun's gravitational parameter, [km ³ /s ²]
ν	= true anomaly, [rad]
ξ	= angle between $\hat{\boldsymbol{t}}$ and $\hat{\boldsymbol{i}}$, [rad]
φ	= polar angle, [rad]
$\boldsymbol{\omega}$	= heliogyro spin rate (with $\omega \triangleq \ \boldsymbol{\omega}\ $), [rad/s]

Subscripts

0	= initial
f	= final
ss	= conventional solar sail
\oplus	= evaluated at 1 au from the Sun

Superscripts

\cdot	= time derivative
\wedge	= unit vector
$-$	= mean value
\sim	= dimensionless
\star	= optimal

1. Introduction

Solar sailing is a fascinating concept of space propulsion that gains thrust from the momentum of solar photons, which are reflected by a large and thin membrane [1, 2, 3]. The heliogyro is a rotating solar sail, whose reflective surface is divided into a number of long and slender blades that are stiffened by a suitable spin-induced centrifugal force [4], as is sketched in Fig. 1. Thanks to such a helicopter-like design, which avoids the use of heavy booms necessary to stiffen the reflective film [5, 6], a heliogyro is potentially able to provide a higher propulsive acceleration magnitude than a conventional (i.e., not rotating, three-axis stabilized, and polygonal) solar sail of equal reflective area and payload mass [7]. Each blade may be rotated around its own longitudinal axis (i.e., the axis extending from the blade root to the blade tip) to obtain

the desired pitch angle, thus allowing the thrust vector to be controlled more effectively than that of a conventional solar sail or a refractive sail [8, 9, 10]. The plane identified by all the longitudinal axes of the blades is here referred to as the fundamental plane of the heliogyro. The spin axis is therefore perpendicular to the fundamental plane and passes through the heliogyro center of mass; see Fig. 1.

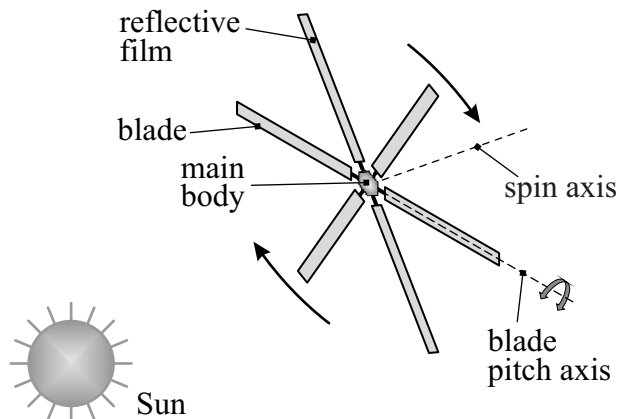


Figure 1: Sketch of heliogyro concept.

The aim of this paper is to present a simplified analysis of the thrust vector provided by a heliogyro and to investigate its capabilities in executing a set of optimal (minimum-time) trajectories for two-dimensional interplanetary transfers. The study is specialized to the case of a heliogyro with a Sun-facing attitude, that is, when the heliogyro fundamental plane is perpendicular to the Sun-spacecraft line. Note that this special configuration would also be useful, for example, to maintain an artificial Lagrangian point [11]. In that case, the problem of determining the optimal control is considerably simplified because the thrust vector orientation of a Sun-facing heliogyro (SFH) only depends on the blade pitch angles. The proposed mathematical model shows that the propulsive acceleration vector of an SFH can be analytically described in a compact form as a function of the number of blades and their orientation only. It is also proved that the mean propulsive acceleration vector over a complete rotation of the SFH about its spin axis is independent of the number of blades and can be expressed as a function of a single control parameter.

The simplified SFH thrust model is then used to study the classical minimum-time rendezvous problem between heliocentric coplanar orbits [12, 8]. To that end, the optimal steering law for an SFH is first determined in closed form, then some exemplary cases (including missions to the asteroid 25143 Itokawa or circle-to-circle Earth-Mars and Earth-Venus transfers) are analyzed using both an indirect method [13, 14, 15] and a semi-analytical approach. Minimum flight times are estimated as a function of the heliogyro characteristic acceleration, defined as the maximum propulsive acceleration at a reference Sun-spacecraft distance of one astronomical unit, which is the design parameter that quantifies the heliogyro performance. In an SFH configuration, the maximum propulsive acceleration occurs when all the blade pitch angles are set to zero, that is, when the blades are at their rest position and, as such, belong to the heliogyro fundamental plane. In that special case, the SFH provides a purely outward radial thrust.

The remainder of the paper is organized as follows. Section 2 is devoted to a brief review of previous works related to the heliogyro concept, while Section 3 presents the analytical thrust model of an SFH. Section 4 analyzes the minimum-time transfer problem and derives the optimal steering law in closed form. The obtained control law is then used in Section 5 for investigating optimal heliocentric transfers in some two-dimensional mission scenarios of interest. Finally, the last section contains some concluding remarks.

2. Heliogyro concept review

The heliogyro concept was first proposed by Astro Research Corporation and MacNeal-Schwendler Corporation [16, 17] in the mid 1960s as a particular solar sail configuration, in which the reflective surface is divided into a number of long and slender blades that resemble the arrangement of a helicopter rotor.

This innovative and rather unconventional sail arrangement was extensively studied during the 1970s at the Jet Propulsion Laboratory [18, 19, 20] in the context of Wright’s [21] visionary idea (which, unfortunately, remained merely a theory on paper) to rendezvous with Halley’s comet by using a solar sail-based spacecraft. In that mission scenario, the performance of a baseline 12-blade heliogyro, in which the size of each rectangular blade was about $8\text{ m} \times 7.5\text{ km}$, was investigated by considering a reflective membrane of aluminum coated Kapton with an infrared emissive coating on the shaded side.

After that first pioneering phase, the interest in scientific research on the heliogyro regained strength at the beginning of the 2010s, as is confirmed by the number of heliogyro-related papers presented at the third International Symposium on Solar Sailing [22]. During that conference, some important issues related to the heliogyro concept were addressed [23], such as the analysis of the dynamic behavior of a spinning blade [24, 25], the study of the heliogyro solar-elastic stability [26], and an investigation of its attitude control via a suitable set of blade pitch maneuvers [27]. In the recent years, an interesting contribution is represented by the works by Guerrant et al. [28, 29, 30, 31], Guerrant and Lawrence [32, 33], and Wilkie et al. [34], who investigated some crucial aspects (on which we do not go into details) related to the blade pitch and torsional dynamics.

In the context of dynamics and orbital control, Heiligers et al. [35] addressed the heliogyro inverse problem (i.e., the problem of determining the blade pitch profile that generates a given thrust and/or torque vector) using a numerical technique and applied such a method to track a reference trajectory that corrects injection errors into a Sun-Earth (sub- L_1) halo orbit. Moreover, Heiligers et al. [36] exploited the force control authority of a heliogyro for studying the orbital control of Sun-Earth (sub- L_1) halo orbits by means of a linear-quadratic feedback controller.

More recently, Pimienta-Peñalver et al. [37] provided an improvement upon the existing discrete-mass models of the heliogyro blade and extended its application from a single membrane blade to a full heliogyro constituted by multiple blades spinning about a rigid central hub. Additionally, they implemented a control algorithm at each blade root to enforce structural integrity and attitude control. Moreover, in Ref. [38] they also established a hybrid approach where the blades are divided into equal sections, in which the mass is lumped into discrete points located at their edges. Subsequently, Kim et al. [39] analyzed a possible control strategy for a full heliogyro deployment by controlling the blade pitch angle and the angular velocity of the blade reel. The simulation results proved that the blades can be successfully deployed at the desired final rotational speed using an open-loop control system. This is certainly a non-trivial result because, during the heliogyro unrolling phase, the increase of its moment of inertia decreases the spacecraft angular velocity. In addition, Juang et al. [40] presented a number of simulation cases that showed how the flutter instability frequencies vary with the solar radiation pressure (SRP) and the dynamic model size, while Kang and Park [41] applied the Floquet stability analysis to a three-dimensional nonlinear blade subjected to time-varying SRP. In particular, they determined the stability boundaries in the domain of SRP and spin rate and in the domain of SRP and angle between the Sun-spacecraft (i.e., radial) line and the heliogyro spin axis. Moreover, Kang and Park [42] investigated the dynamic behavior of a flexible multibody heliogyro solar sail (consisting of a central rigid body and six flexible solar blades subject to SRP and gravitational forces) using a floating frame approach. The proposed model [42] was then applied to demonstrate the feasibility of Sun-synchronous orbits around the Earth.

Finally, Cook et al. [43] performed damping characterization tests on small-scale heliogyro blades hanging in a high-vacuum chamber and managed to calculate separate flap and twist damping ratios for the first three modes. The obtained results led to the conclusion that a linear viscous torsional blade damping model is inadequate for the design of a robust proximal blade twist feedback controller. Then, Cook and Lawrence [44] elaborated three modal damping models based on the previous experimental data and integrated them into a single blade heliogyro model. They found out that a proximal blade twist feedback controller is able to satisfy the settling time requirement for a heliogyro technology demonstration mission.

In essence, the reason why the heliogyro concept is still capturing the attention of researchers and, therefore, it is worthy of further investigation, is that its performance is relatively higher than that of a conventional solar sail of equal reflective area and payload mass. This property is a result of the centrifugal force obtained by spinning the heliogyro around a rotation axis, thanks to which the blades are stiffened and mechanically stabilized without the need of any massive booms that would otherwise be required to support a non-rotating membrane. In other terms, the reflective surface area and the payload mass being the same, the lower structural mass of a heliogyro guarantees a higher propulsive acceleration magnitude. This point

is emphasized in Guerrant’s doctoral thesis [45], which is a rich source of references useful to start a general research about the heliogyro concept.

3. Simplified models for thrust and torque vectors

Consider a heliogyro-based spacecraft of total mass m that rotates with a constant angular velocity $\boldsymbol{\omega}$ at a distance $r \triangleq \|\mathbf{r}\|$ from the Sun, where \mathbf{r} is the Sun-spacecraft position vector. The heliogyro is made up of $N \geq 2$ rectangular and double-reflective blades of equal size, with length l and width $w \ll l$.

In this analysis the blades are modelled as rigid and perfectly reflective membranes, which implies that the incident light is specularly reflected [21]. Actually, the blades are not rigid and their torsional bending causes the twist at the tip to be less than the twist at the root. This unwanted structural behaviour had already been observed during MacNeal’s pioneering work [17], in which the author came to the conclusion that the blade trim can be maintained by controlling the chordwise relative locations of the center of pressure and center of gravity. The assumption of rigid blades is however made here to simplify the following analysis and to provide an analytical description of the thrust and torque vectors generated by a heliogyro.

It is now useful to introduce a radial-tangential-normal (orbital) reference frame $\mathcal{T}_O(C; \hat{\mathbf{i}}_O, \hat{\mathbf{j}}_O, \hat{\mathbf{k}}_O)$, centered at the spacecraft center of mass C , in which $\hat{\mathbf{k}}_O \equiv \hat{\mathbf{r}} \triangleq \mathbf{r}/r$ is along the Sun-spacecraft line, $\hat{\mathbf{j}}_O$ is directed along the specific angular momentum vector $\mathbf{h} \triangleq \mathbf{r} \times \mathbf{v}$ (where \mathbf{v} is the spacecraft inertial velocity vector), and $\hat{\mathbf{i}}_O$ completes the right-handed coordinate system; see Fig. 2. Note that the plane $(\hat{\mathbf{i}}_O, \hat{\mathbf{j}}_O)$ coincides with the local horizontal plane.

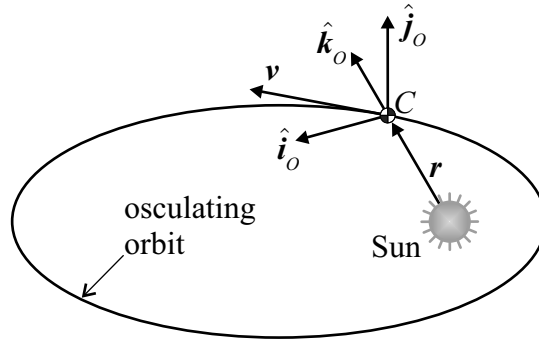


Figure 2: Radial-tangential-normal reference frame.

Furthermore, let $\mathcal{T}_B(C; \hat{\mathbf{i}}, \hat{\mathbf{j}}, \hat{\mathbf{k}})$ be a body reference frame with $\hat{\mathbf{k}}$ parallel to the heliogyro spin axis, in such a way that $\boldsymbol{\omega} \triangleq \omega \hat{\mathbf{k}}$, where ω is the spacecraft spin rate. Note that the heliogyro fundamental plane is identified by the unit vectors $\hat{\mathbf{i}}$ and $\hat{\mathbf{j}}$. Figure 3 sketches a simplified heliogyro with 4 blades. The generic blade orientation is described with the aid of a blade-fixed (right-handed) reference frame $\mathcal{T}_k(C_k; \hat{\mathbf{i}}_k, \hat{\mathbf{j}}_k, \hat{\mathbf{k}}_k)$ with $k = \{1, \dots, N\}$, where C_k represents the k -th blade center of mass, $\hat{\mathbf{i}}_k$ (with $\hat{\mathbf{i}}_1 \equiv \hat{\mathbf{i}}$) is parallel to the rotation axis of the k -th blade and is oriented towards the blade tip, and $\hat{\mathbf{k}}_k$ is orthogonal to the blade surface and points in the same direction as $\hat{\mathbf{k}}$ when the blade is at its rest position, as shown in Fig. 3.

The SRP-induced thrust \mathbf{F}_k generated by the k -th blade can be described by means of an ideal force model [1], that is

$$\mathbf{F}_k = \frac{2P A_{\text{tot}}}{N} \left| \hat{\mathbf{r}} \cdot \hat{\mathbf{k}}_k \right| \left(\hat{\mathbf{r}} \cdot \hat{\mathbf{k}}_k \right) \hat{\mathbf{k}}_k \quad (1)$$

where $A_{\text{tot}} \triangleq N l w$ is the total reflective area, $\hat{\mathbf{r}}$ is the radial unit vector, and P is the local SRP, given by

$$P = P_{\oplus} \left(\frac{r_{\oplus}}{r} \right)^2 \quad (2)$$

where $P_{\oplus} \simeq 4.54 \mu\text{Pa}$ is the value of P at the reference distance $r_{\oplus} \triangleq 1 \text{ au}$. Note that $\mathbf{F}_k \cdot \hat{\mathbf{r}} \geq 0$ whatever the orientation of \mathcal{T}_B and \mathcal{T}_k is. Bearing in mind Eq. (1), the propulsive acceleration vector \mathbf{a} provided by

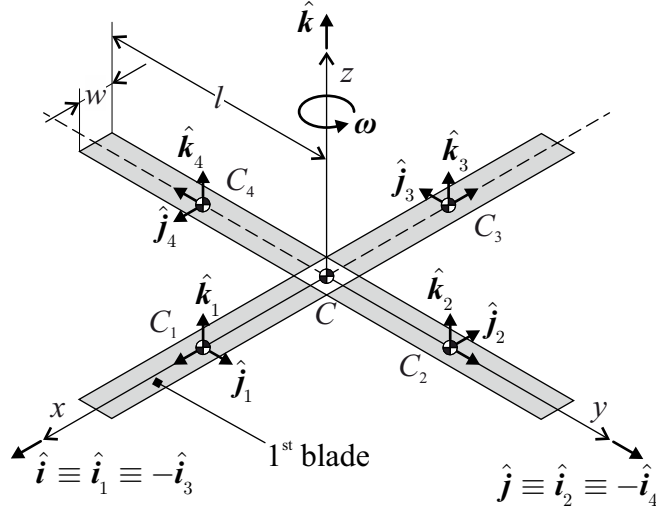


Figure 3: Conceptual scheme of a heliogyro with $N = 4$.

the heliogyro is

$$\mathbf{a} = \frac{1}{m} \sum_{k=1}^N \mathbf{F}_k \quad (3)$$

which can be rewritten as

$$\mathbf{a} = a_c \left(\frac{r_{\oplus}}{r} \right)^2 \frac{1}{N} \sum_{k=1}^N \left| \hat{\mathbf{r}} \cdot \hat{\mathbf{k}}_k \right| \left(\hat{\mathbf{r}} \cdot \hat{\mathbf{k}}_k \right) \hat{\mathbf{k}}_k \quad (4)$$

where

$$a_c \triangleq \frac{2 P_{\oplus} A_{\text{tot}}}{m} \quad (5)$$

is the characteristic acceleration, that is, the typical performance parameter of a conventional solar sail-based spacecraft.

The propulsive acceleration vector in Eq. (4) can be expressed as a function of the spacecraft attitude relative to \mathcal{T}_O and the blade pitch angles. To this end, the Sun-spacecraft unit vector $\hat{\mathbf{r}}$ is described in \mathcal{T}_B by means of the cone (α_n) and clock (δ_n) angles, such that

$$\hat{\mathbf{r}} = \sin \alpha_n \cos \delta_n \hat{\mathbf{i}} + \sin \alpha_n \sin \delta_n \hat{\mathbf{j}} + \cos \alpha_n \hat{\mathbf{k}} \quad (6)$$

where $\alpha_n \in [0, \pi]$ rad is the angle between $\hat{\mathbf{r}}$ and $\hat{\mathbf{k}}$, while $\delta_n \in [0, 2\pi)$ rad is the angle between $\hat{\mathbf{i}}$ and the projection of $\hat{\mathbf{r}}$ onto the fundamental plane ($\hat{\mathbf{i}}, \hat{\mathbf{j}}$); see Fig. 4.

Moreover, the unit vector $\hat{\mathbf{k}}_k$ may be written as a function of the blade pitch angle and its angular position (i.e., the blade azimuthal location) along the heliogyro fundamental plane as

$$\hat{\mathbf{k}}_k \triangleq \sin \theta_k \sin \zeta_k \hat{\mathbf{i}} - \sin \theta_k \cos \zeta_k \hat{\mathbf{j}} + \cos \theta_k \hat{\mathbf{k}} \quad (7)$$

where $\theta_k \in [-\pi/2, \pi/2]$ rad is the blade pitch angle, while $\zeta_k \triangleq 2\pi(k-1)/N$ represents the azimuth angle (measured counterclockwise starting from $\hat{\mathbf{i}}$) of the k -th blade longitudinal axis on the plane ($\hat{\mathbf{i}}, \hat{\mathbf{j}}$); see Fig. 5.

From Eqs. (6)-(7), the scalar product $\hat{\mathbf{r}} \cdot \hat{\mathbf{k}}_k$ of Eq. (3) becomes

$$\hat{\mathbf{r}} \cdot \hat{\mathbf{k}}_k = \sin \alpha_n \cos \delta_n \sin \theta_k \sin \zeta_k - \sin \alpha_n \sin \delta_n \sin \theta_k \cos \zeta_k + \cos \alpha_n \cos \theta_k \quad (8)$$

so that the propulsive acceleration vector \mathbf{a} is a function of the spacecraft attitude (through the angles α_n and δ_n) and the pitch angle of the generic blade.

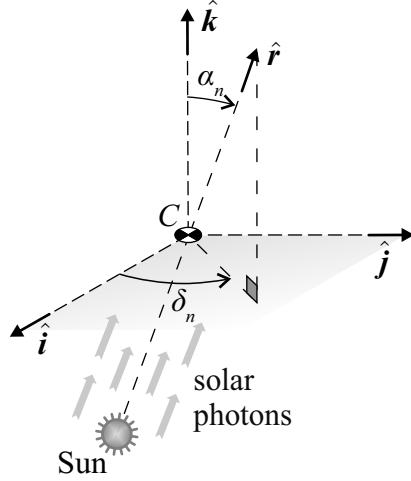


Figure 4: Representation of cone (α_n) and clock (δ_n) angles.

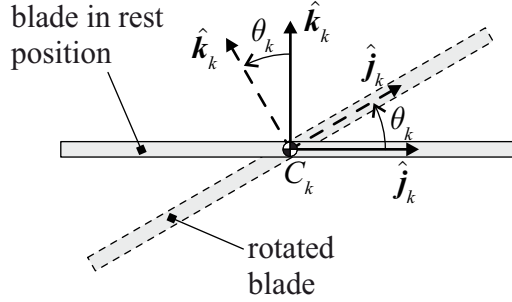


Figure 5: Representation of the generic blade pitch angle θ_k .

3.1. SFH thrust vector mathematical model

The expression of \mathbf{a} , obtained by combining Eqs. (4) and (7)-(8), can be simplified by considering the special but important case of an SFH, which corresponds to when the spacecraft spin axis is parallel to the Sun-spacecraft line, the latter coinciding with the direction of $\hat{\mathbf{r}}$. In this case $\hat{\mathbf{k}} = \hat{\mathbf{k}}_O \equiv \hat{\mathbf{r}}$, the plane $(\hat{\mathbf{i}}, \hat{\mathbf{j}})$ coincides with the local horizontal plane $(\hat{\mathbf{i}}_O, \hat{\mathbf{j}}_O)$, and $\alpha_n = 0$. Therefore, Eq. (8) gives $\hat{\mathbf{r}} \cdot \hat{\mathbf{k}}_k = \cos \theta_k$, and Eq. (3) reduces to the following compact form

$$\mathbf{a} = a_c \left(\frac{r_\oplus}{r} \right)^2 \frac{1}{N} \sum_{k=1}^N \cos^2 \theta_k \hat{\mathbf{k}}_k \quad (9)$$

As a result, an SFH generates a purely radial propulsive acceleration when, for all k , $\theta_k = 0$. In that case, $\mathbf{a} = a_c (r_\oplus/r)^2 \hat{\mathbf{k}}_k$ with $\hat{\mathbf{k}}_k = \hat{\mathbf{k}} \equiv \hat{\mathbf{r}}$. On the other hand, a transverse (that is, which lies on the local horizontal plane) component of \mathbf{a} can be obtained by suitably changing the generic blade pitch angle θ_k .

From the control viewpoint, four different strategies are usually identified in the literature to maneuver an SFH [17, 46]. More precisely, the cyclic pitch maneuver gives a nonzero component of the heliogyro thrust in the $(\hat{\mathbf{i}}, \hat{\mathbf{j}})$ plane while keeping the spacecraft spin rate at a roughly constant value. The collective-cyclic pitch maneuver, instead, produces a radial thrust (that is, a thrust vector directed along $\hat{\mathbf{k}}$) and a steady torque along both the $(\hat{\mathbf{i}}, \hat{\mathbf{j}})$ plane and the $\hat{\mathbf{k}}$ -axis, while the collective pitch maneuver gives rise to a torque and a modulation of the radial thrust component. Finally, the so called half-p pitch maneuver [46] is similar to the collective-cyclic pitch, but does not change the heliogyro spin rate and has a zero net collective pitch component. In this paper, a generalization of the collective-cyclic pitch maneuver is used to obtain a simple

thrust vector mathematical model of an SFH. It will be shown that, with the control strategy used for the generation of the required thrust, the resulting disturbing torque is (at least on average) equal to zero.

Consider now a generic transverse direction $\hat{\mathbf{t}}$, fixed in the local horizontal plane $(\hat{\mathbf{i}}_O, \hat{\mathbf{j}}_O)$, and assume that any blade rotation at an angle θ_k occurs instantaneously. Such an assumption of a “step-like” variation of the blade pitch angle is very useful to simplify the mathematical model, but is rather non-conservative in a real control law design. In fact, flexible heliogyro blades cannot handle a step-like pitch variation because it would excite the structural modes. In practice, a smooth blade pitch variation can be used to get to the overall effect of the (ideal) step-like variation.

Because the heliogyro spins about $\hat{\mathbf{k}}$ at a constant angular rate ω , the components of the transverse unit vector $\hat{\mathbf{t}}$ in the body frame \mathcal{T}_B are

$$\hat{\mathbf{t}} \triangleq \cos \xi \hat{\mathbf{i}} + \sin \xi \hat{\mathbf{j}} \quad \text{with} \quad \xi \triangleq \xi_0 - \omega t \quad (10)$$

where ξ is the angle between $\hat{\mathbf{t}}$ and $\hat{\mathbf{i}}$, t is the time, and $\xi_0 \triangleq \xi(t_0)$ is the value of ξ at $t_0 \triangleq 0$; see Fig. 6.

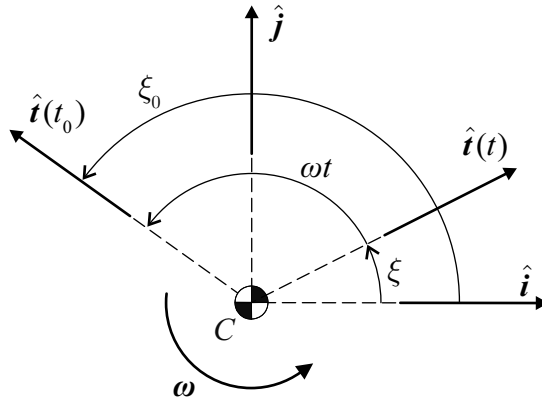


Figure 6: Sketch of unit vector $\hat{\mathbf{t}}$.

The maximum value of the component of \mathbf{a} along $\hat{\mathbf{t}}$ can be obtained, at a generic time instant t , by finding the angle $\theta_k = \theta_k(t)$ that maximizes the dot product $a_t \triangleq \mathbf{a} \cdot \hat{\mathbf{t}}$, which, from Eqs. (9)-(10), is

$$a_t = a_c \left(\frac{r_{\oplus}}{r} \right)^2 \frac{1}{N} \sum_{k=1}^N \cos^2 \theta_k \sin \theta_k \sin (\zeta_k - \xi) \quad (11)$$

From the previous equation, the value of a_t is maximum when

$$\theta_k = \theta_k^* \triangleq \text{sign} (\sin (\zeta_k - \xi)) \arccos \left(\sqrt{2/3} \right) \quad (12)$$

so that the expression of \mathbf{a} when $\theta_k = \theta_k^*$ can be written in a compact form as

$$\mathbf{a}(\theta_k^*) \triangleq \mathbf{a}^* = a_r^* \hat{\mathbf{r}} + a_t^* \hat{\mathbf{t}} + a_p^* \hat{\mathbf{p}} \quad (13)$$

where $\hat{\mathbf{p}} \triangleq \hat{\mathbf{r}} \times \hat{\mathbf{t}} \equiv -\sin \xi \hat{\mathbf{i}} + \cos \xi \hat{\mathbf{j}}$ and

$$a_r^* \triangleq a_c \left(\frac{r_{\oplus}}{r} \right)^2 \frac{2\sqrt{6}}{9} \quad (14)$$

$$a_t^* \triangleq a_c \left(\frac{r_{\oplus}}{r} \right)^2 \frac{2\sqrt{3}}{9N} \sum_{k=1}^N |\sin (\zeta_k - \xi)| \quad (15)$$

$$a_p^* \triangleq -a_c \left(\frac{r_{\oplus}}{r} \right)^2 \frac{2\sqrt{3}}{9N} \sum_{k=1}^N \text{sign} (\sin (\zeta_k - \xi)) \cos (\zeta_k - \xi) \quad (16)$$

Note that a_r^* is independent of ξ (or t), while both a_t^* and a_p^* change with ξ , as is shown in Fig. 7, where $\{\tilde{a}_t^*, \tilde{a}_p^*\}$ are dimensionless terms, defined as

$$\tilde{a}_t^* \triangleq \frac{a_t^*}{a_c \left(\frac{r_\oplus}{r}\right)^2}, \quad \tilde{a}_p^* \triangleq \frac{a_p^*}{a_c \left(\frac{r_\oplus}{r}\right)^2} \quad (17)$$

In particular, the period of \tilde{a}_t^* and \tilde{a}_p^* is $2\pi/N$ rad when N is even, while it is π/N rad when N is odd.

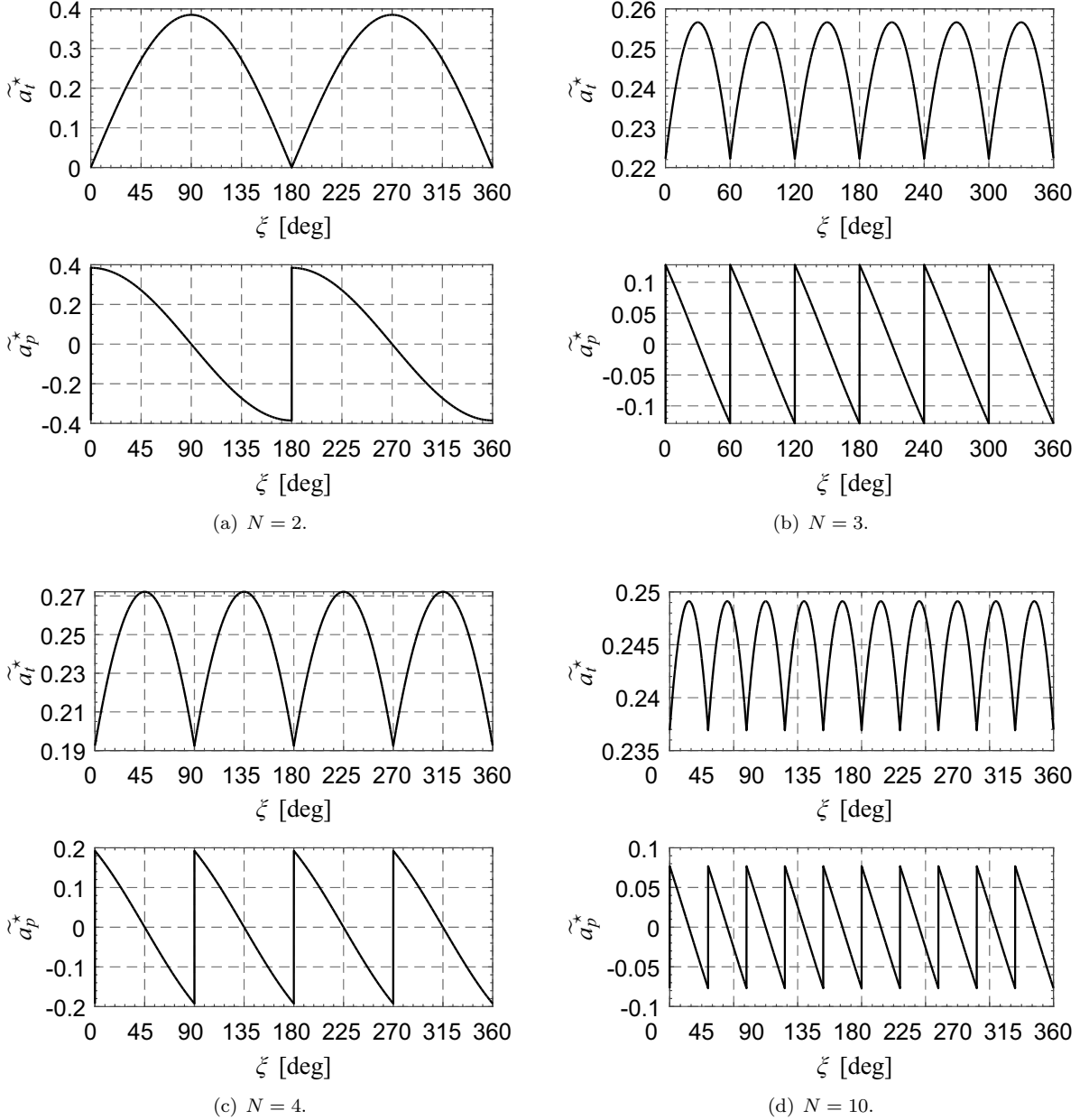


Figure 7: Variation of \tilde{a}_t^* and \tilde{a}_p^* with ξ and N .

The maximum and minimum values of $\{\tilde{a}_t^*, \tilde{a}_p^*\}$ are plotted in Fig. 8 as a function of N . The figure shows that the values of \tilde{a}_t^* (or \tilde{a}_p^*) converge to approximately 0.245 (or 0) as N increases. These limiting values

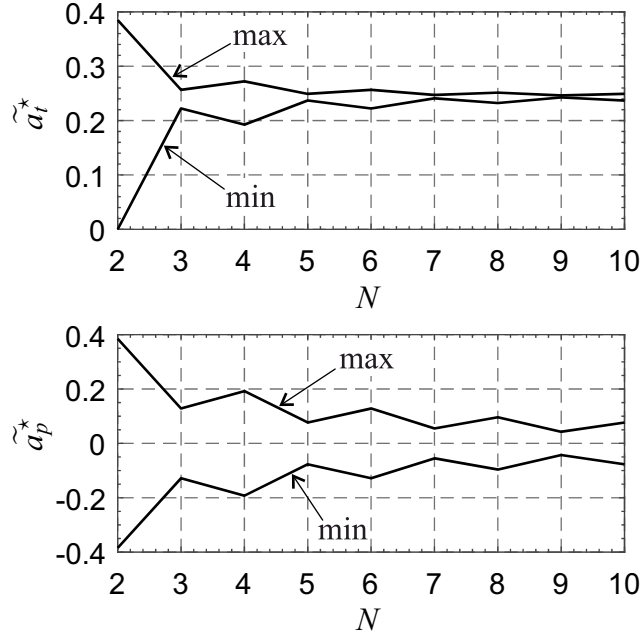


Figure 8: Maximum and minimum values of \tilde{a}_t^* and \tilde{a}_p^* as a function of N .

coincide with the dimensionless forms of the mean values of $\{a_t^*, a_p^*\}$, denoted as $\{\bar{a}_t^*, \bar{a}_p^*\}$, during a heliogyro rotation period $2\pi/\omega$. In fact, the mean values $\{\bar{a}_t^*, \bar{a}_p^*\}$ can be obtained from Eqs. (15)-(16) as

$$\bar{a}_t^* \triangleq \frac{1}{T} \int_0^T a_t^* dt = a_c \left(\frac{r_\oplus}{r}\right)^2 \frac{4\sqrt{3}}{9\pi} \quad (18)$$

$$\bar{a}_p^* \triangleq \frac{1}{T} \int_0^T a_p^* dt = 0 \quad (19)$$

where $4\sqrt{3}/(9\pi) \simeq 0.245$. In other terms, when the orientation of the generic blade is such to maximize the projection of \mathbf{a} along the transverse unit vector $\hat{\mathbf{t}}$, the mean value of the propulsive acceleration vector can be written as

$$\bar{\mathbf{a}}^* \triangleq \frac{1}{T} \int_0^T \mathbf{a}^* dt = a_r^* \hat{\mathbf{r}} + \bar{a}_t^* \hat{\mathbf{t}} \quad (20)$$

where a_r^* and \bar{a}_t^* are given by Eqs. (14) and (18), respectively.

The previous results may be easily adapted to the more general case when the blade pitch angle is in the form

$$\theta_k = \text{sign}(\sin(\zeta_k - \xi)) \vartheta \quad (21)$$

where $\vartheta \in [-\pi/2, \pi/2]$ rad is a control parameter. In this case, the mean propulsive acceleration vector, defined as

$$\bar{\mathbf{a}} \triangleq \frac{1}{T} \int_0^T \mathbf{a} dt \quad (22)$$

belongs to the plane $(\hat{\mathbf{r}}, \hat{\mathbf{t}})$ and its components depend on the assigned value of ϑ . In particular, when $\vartheta = 0$, the propulsive acceleration vector is purely radial, while the component of $\bar{\mathbf{a}}$ along the transverse unit vector $\hat{\mathbf{t}}$ is maximized (or minimized) when $\vartheta = \arccos(\sqrt{2/3})$ rad (or $\vartheta = -\arccos(\sqrt{2/3})$ rad). Note that, in a real mission scenario, when the actual blade control capability must necessarily be taken into account, a sinusoidal cyclic amplitude of about 42 deg may be chosen as it maximizes the transverse propulsive acceleration, yielding a normalized magnitude of about 0.2246 [33].

For a generic value of ϑ , the mean propulsive acceleration is therefore

$$\bar{\mathbf{a}} = a_r \hat{\mathbf{r}} + \bar{a}_t \hat{\mathbf{t}} \quad (23)$$

where

$$a_r \triangleq a_c \left(\frac{r_\oplus}{r} \right)^2 \cos^3 \vartheta \quad , \quad \bar{a}_t \triangleq a_c \left(\frac{r_\oplus}{r} \right)^2 \frac{2}{\pi} \cos^2 \vartheta \sin \vartheta \quad (24)$$

The mean value of Eq. (23) will now be used in place of the instantaneous one given by Eq. (9), because the heliogyro rotation period is considerably smaller than the characteristic time scale of a heliocentric orbital motion. Note that the transverse component of $\bar{\mathbf{a}}$ is multiplied by a factor $2/\pi \simeq 0.637$ when compared to the case of a conventional solar sail without attitude constraints [47] and optical degradation [48, 49, 50] if, in the latter case, ϑ represents the angle between $\hat{\mathbf{r}}$ and the normal to the sail fundamental plane in the direction opposite to the Sun. Furthermore, the thrust angle α (that is, the angle between $\bar{\mathbf{a}}$ and $\hat{\mathbf{r}}$) is given by

$$\alpha = \arctan \left(\frac{2}{\pi} \tan \vartheta \right) \quad (25)$$

and is shown in Fig. 9.

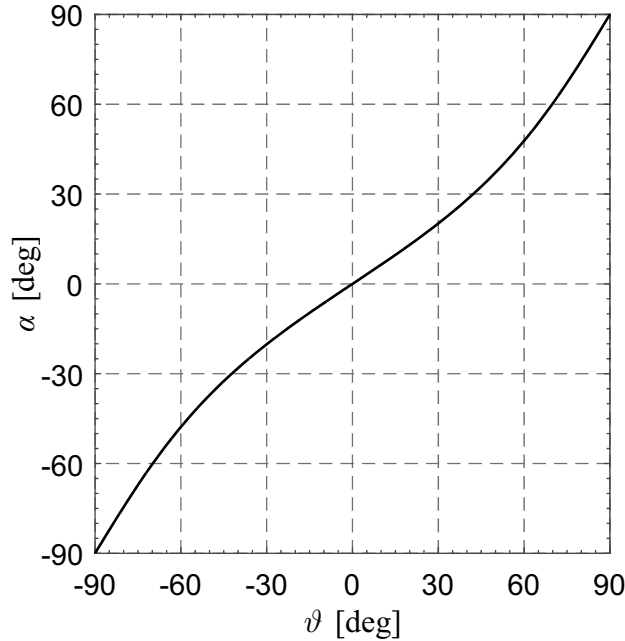


Figure 9: Variation of the thrust angle α with ϑ .

A final remark concerns the maximum transverse component of the mean propulsive acceleration vector. While for a solar sail it occurs when $\alpha = \arctan(1/\sqrt{2})$ rad $\simeq 35.26$ deg, an SFH generates its maximum transverse acceleration when $\alpha = \arctan(\sqrt{2}/\pi)$ rad $\simeq 24.24$ deg; see Fig. 10, where

$$\tilde{a}_r \triangleq \frac{a_r}{a_c \left(\frac{r_\oplus}{r} \right)^2} \quad , \quad \tilde{a}_t \triangleq \frac{\bar{a}_t}{a_c \left(\frac{r_\oplus}{r} \right)^2} \quad (26)$$

The lack of an overline in \tilde{a}_r emphasizes that it is not a mean value since, as stated, the radial acceleration is independent of time. Note that the expressions of \tilde{a}_r and \tilde{a}_t may also be rewritten from Eq. (23) using α as the independent variable, and the result is

$$\tilde{a}_r = \left[\left(\frac{\pi}{2} \tan \alpha \right)^2 + 1 \right]^{-3/2} \quad , \quad \tilde{a}_t = \tilde{a}_r \tan \alpha \quad (27)$$

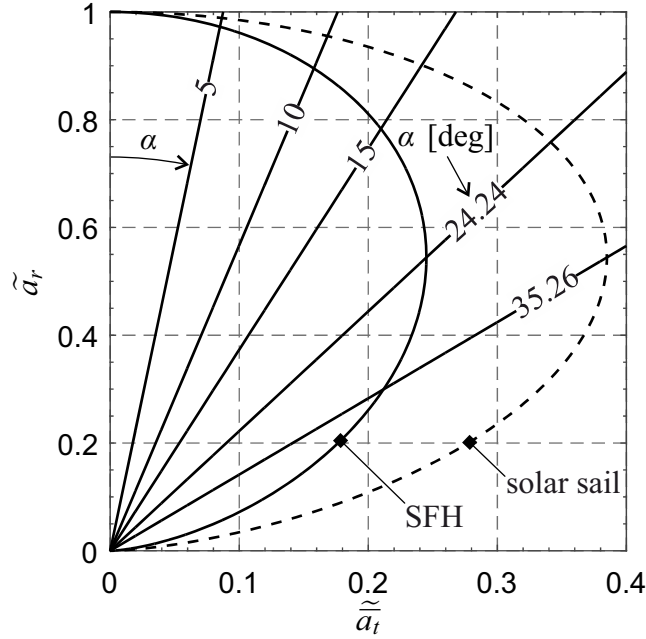


Figure 10: Variation of \tilde{a}_r with \tilde{a}_t and corresponding α for an SFH (solid line) and a flat solar sail without attitude constraints (dotted line).

3.2. SFH torque vector

The generation of a propulsive acceleration gives rise to a disturbing torque acting on the heliogyro. For a SFH, the torque due to a single blade is

$$\mathbf{M}_k = -\frac{2PA_{\text{tot}}}{N} \left[\frac{l}{2} + \frac{w}{2} \cot\left(\frac{\pi}{N}\right) \right] \cos^2 \theta_k \hat{\mathbf{j}}_k \quad (28)$$

where $\hat{\mathbf{j}}_k \triangleq -\cos \theta_k \sin \zeta_k \hat{\mathbf{i}} + \cos \theta_k \cos \zeta_k \hat{\mathbf{j}} + \sin \theta_k \hat{\mathbf{k}}$. The total torque vector is therefore

$$\mathbf{M} = \sum_{k=1}^N \mathbf{M}_k \quad (29)$$

Using the control law given by Eq. (21), it may be verified that $\mathbf{M} = \mathbf{0}$ when N is even, while

$$\mathbf{M} = \frac{2PA_{\text{tot}}}{N} \left[\frac{l}{2} + \frac{w}{2} \cot\left(\frac{\pi}{N}\right) \right] \cos^2 \vartheta \sin \vartheta \text{sign}(\sin(N\xi)) \hat{\mathbf{k}} \quad (30)$$

when N is odd. In the latter case, the mean value of \mathbf{M} is

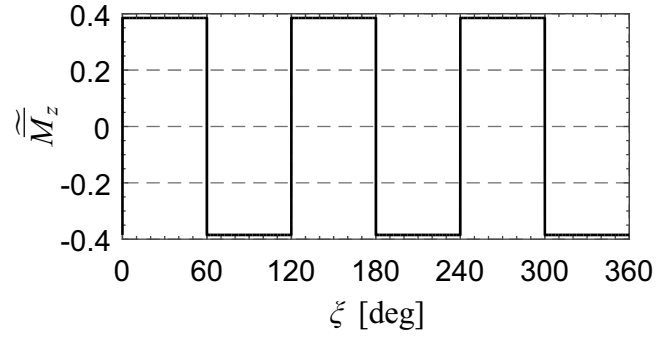
$$\overline{\mathbf{M}} \triangleq \frac{1}{T} \int_0^T \mathbf{M} dt = 0 \quad (31)$$

Figure 11 shows the function $\widetilde{M}_z \triangleq \cos^2 \vartheta \sin \vartheta \text{sign}(\sin(N\xi))$ when $N = \{3, 5\}$ and $\vartheta = \arccos(\sqrt{2/3})$ rad.

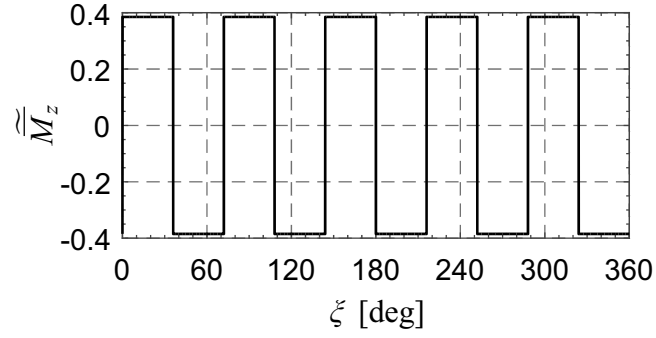
It is worth noting that, if N is odd, the period of \widetilde{M}_z is $2\pi/N$. In conclusion, the disturbing torque is (at least on average) equal to zero. Notably, this result is in agreement with the models discussed by Blomquist [46].

4. Trajectory optimization

Minimum-time transfer trajectories of an SFH-based spacecraft between two heliocentric coplanar orbits are now investigated using an indirect approach. To that end, introduce a heliocentric polar reference frame



(a) $N = 3$.



(b) $N = 5$.

Figure 11: Variation of \widetilde{M}_z with ξ and N .

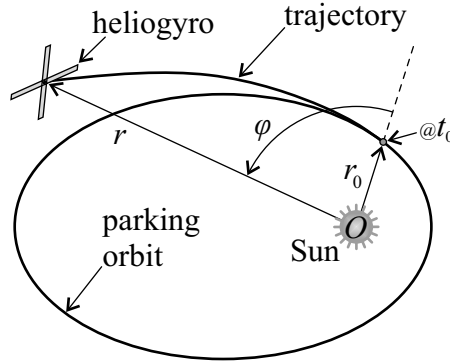


Figure 12: Heliocentric polar reference frame.

$\mathcal{T}_\odot(O; \hat{r}, \hat{t})$, with its origin at the Sun's center of mass O , where the spacecraft polar angle φ is measured from the Sun-spacecraft direction at the initial time t_0 ; see Fig. 12.

The two-dimensional motion of the SFH-based spacecraft may be described in \mathcal{T}_\odot through the following

system of nonlinear equations

$$\dot{r} = v_r \quad (32)$$

$$\dot{\varphi} = \frac{v_\varphi}{r} \quad (33)$$

$$\dot{v}_r = -\frac{\mu_\odot}{r^2} + \frac{v_\varphi^2}{r} + a_r \quad (34)$$

$$\dot{v}_\varphi = -\frac{v_r v_\varphi}{r} + \bar{a}_t \quad (35)$$

where μ_\odot is the Sun's gravitational parameter, v_r (or v_φ) is the radial (or the transverse) component of the spacecraft inertial velocity, and a_r (or \bar{a}_t) is the radial (or the transverse) component of the mean propulsive acceleration vector given by Eqs. (24).

Minimum-time trajectories may be analyzed by maximizing, at any time, the Hamiltonian function associated to the problem. This procedure is not reported here, as it is thoroughly described elsewhere [14, 51, 52]. It is well known [13] that the optimal control law that solves this kind of problem maximizes, at any time, the projection of the propulsive acceleration vector along the direction of Lawden's primer vector [53]. Let the primer vector be parallel to the unit vector $\hat{\mathbf{d}}$, defined as

$$\hat{\mathbf{d}} \triangleq \cos \alpha_d \hat{\mathbf{r}} + \sin \alpha_d \hat{\mathbf{t}} \quad (36)$$

where $\alpha_d \in [-\pi, \pi]$ rad is the angle between $\hat{\mathbf{d}}$ and $\hat{\mathbf{r}}$; see Fig. 13. The optimal control law $\vartheta = \vartheta^*$ (or,

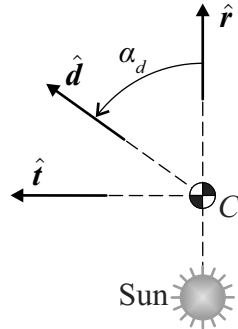


Figure 13: Sketch $\hat{\mathbf{d}}$ and α_d .

equivalently, $\alpha = \alpha^*$) maximizes, at any time, the projection of $\bar{\mathbf{a}}$ along $\hat{\mathbf{d}}$ [53]. The expression of ϑ^* can be obtained, in an analytical and compact form, by introducing the dimensionless cost function $\mathcal{J} = \mathcal{J}(\vartheta, \alpha_d)$, defined as

$$\mathcal{J} \triangleq \frac{\bar{\mathbf{a}} \cdot \hat{\mathbf{d}}}{a_c \left(\frac{r_\oplus}{r}\right)^2} = \cos^2 \vartheta \left(\cos \vartheta \cos \alpha_d + \frac{2}{\pi} \sin \vartheta \sin \alpha_d \right) \quad (37)$$

and enforcing the necessary condition

$$\frac{\partial \mathcal{J}}{\partial \vartheta} = 0 \quad (38)$$

From Eqs. (37)-(38), neglecting the trivial solutions $\vartheta = \pm\pi/2$ rad, the optimal value of the control parameter ϑ is given by

$$\vartheta^* = \frac{\gamma - \arcsin\left(\frac{\sin \gamma}{3}\right)}{2} \quad (39)$$

where the auxiliary angle $\gamma \in [0, 2\pi)$ rad is defined such that

$$\sin \gamma \triangleq \frac{2 \sin \alpha_d}{\sqrt{4 \sin^2 \alpha_d + \pi^2 \cos^2 \alpha_d}} \quad , \quad \cos \gamma \triangleq \frac{\pi \cos \alpha_d}{\sqrt{4 \sin^2 \alpha_d + \pi^2 \cos^2 \alpha_d}} \quad (40)$$

Note that the optimal value of the SFH thrust angle α^* can be obtained from Eqs. (25)-(39) as

$$\alpha^* = \arctan \left[\frac{2}{\pi} \tan \left(\frac{\gamma - \arcsin \left(\frac{\sin \gamma}{3} \right)}{2} \right) \right] \quad (41)$$

which is drawn in Fig. 14, along with ϑ^* , as a function of α_d .

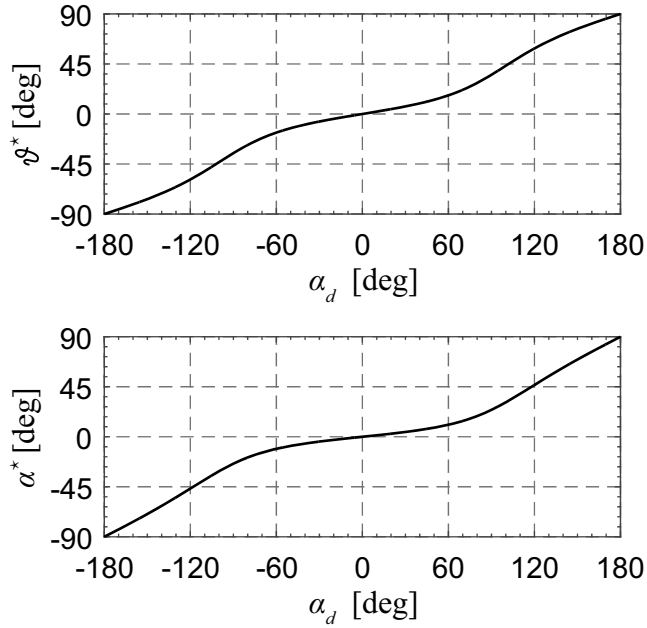


Figure 14: Variation of the optimal values ϑ^* and α^* with α_d .

For the sake of completeness, the optimal thrust angle given by Eq. (41) is compared to that of a conventional solar sail without attitude constraints (here referred to as α_{ss}^*), which, according to Sauer [13], is

$$\alpha_{ss}^* = \arctan \left(\frac{\sqrt{8 + \cos^2 \alpha_d} - 3 \cos \alpha_d}{4 \sin \alpha_d} \right) \quad (42)$$

The comparison between the functions $\alpha^*(\alpha_d)$ and $\alpha_{ss}^*(\alpha_d)$ is shown in Fig. 15.

5. Case studies

The proposed thrust model and optimal control law are used to analyze a set of heliocentric two-dimensional transfers. For exemplary purposes, the SFH heliocentric parking orbit is assumed to be circular with radius $r_0 = r_{\oplus}$. This scenario is consistent with that of a heliogyro that leaves the Earth's sphere of influence on a parabolic escape trajectory, with the simplifying assumption that the planetary orbit is circular.

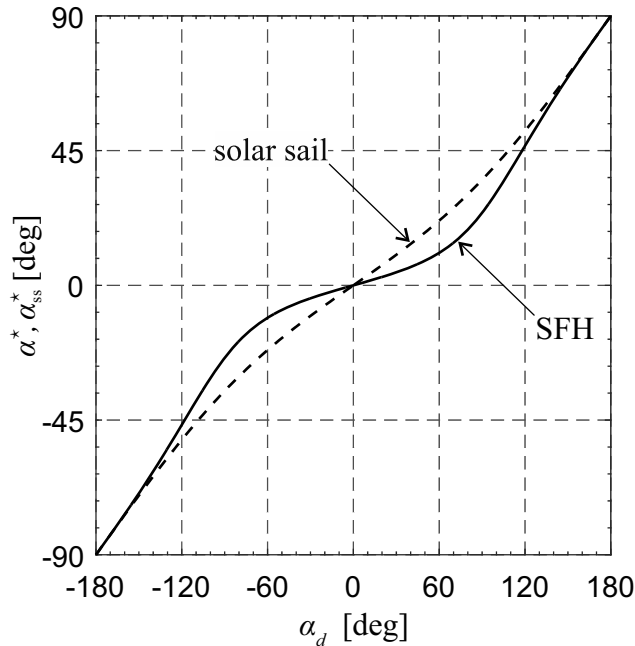


Figure 15: Comparison between the optimal steering laws of an SFH (solid line) and a flat solar sail without attitude constraints (dotted line).

5.1. Earth-Mars and Earth-Venus circle-to-circle orbit transfers

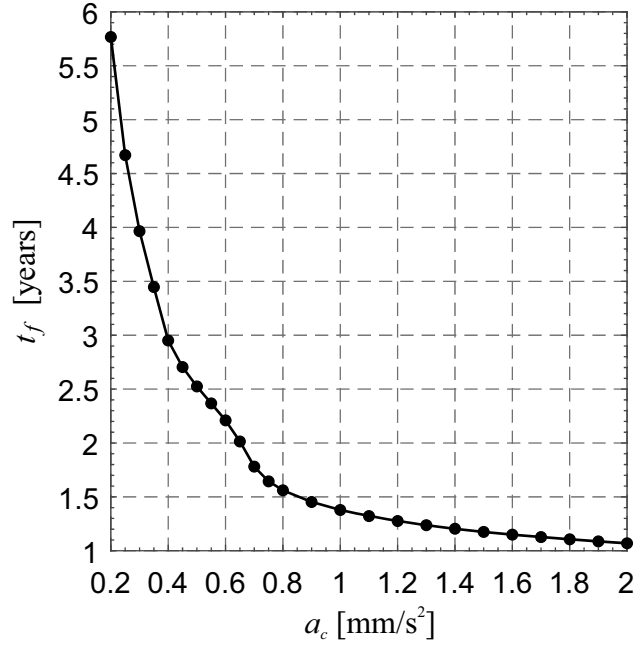
Consider a generic circle-to-circle heliocentric transfer between two coplanar orbits, and assume that the target orbit radius is $r_f = 1.523$ au (or $r_f = 0.723$ au). This case is consistent with an ephemeris-free Earth-Mars (or Earth-Venus) transfer, in which the eccentricity and the mutual inclination between the planetary orbits are both neglected.

The optimal transfer has been analyzed with a spacecraft characteristic acceleration ranging in the interval $[0.2, 2]$ mm/s², and the variation of the minimum flight time t_f with a_c has been drawn in Fig. 16. In particular, Fig. 16(a) (or Fig. 16(b)) shows that t_f increases rapidly when a_c becomes less than 0.7 mm/s² (or less than 0.6 mm/s²) in a Earth-Mars (or Earth-Venus) mission scenario. Figures 17 and 18 show in more detail the cases $a_c = 0.2$ mm/s² and $a_c = 2$ mm/s² for the two mission scenarios, in terms of transfer trajectory and optimal control law.

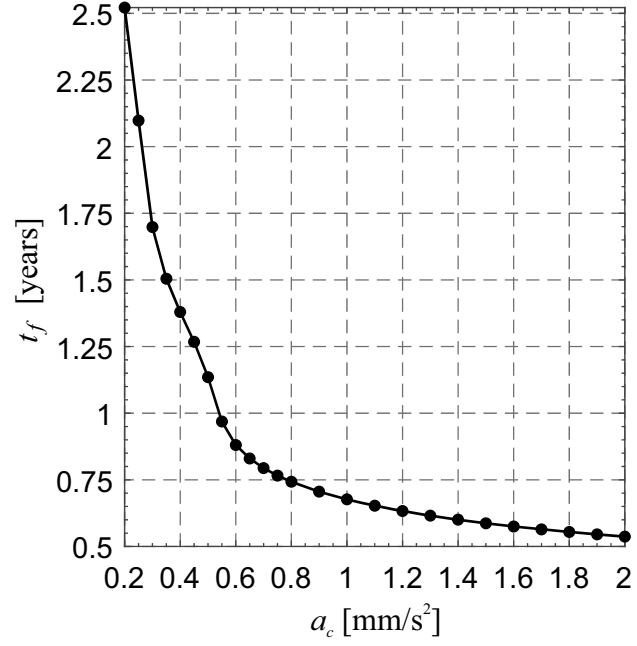
5.2. Circle-to-circle transfer with low-performance SFH

When dealing with circle-to-circle orbit transfers using a low-performance SFH, the optimal transfer duration can be related to the characteristic acceleration through an analytical approximation. Such a relationship is now obtained by paralleling the procedure discussed by Quarta and Mengali [54], who developed an analytical model for estimating the minimum flight time and the number n of revolutions around the Sun required by a low performance solar sail without attitude constraints to perform a circle-to-circle orbit transfer. In particular, for given values of r_0 and r_f , Quarta and Mengali [54] showed that t_f is inversely proportional to a_c when a_c is sufficiently small (i.e., when the number of revolutions around the Sun is sufficiently high). In those cases, they observed that $v_r \simeq 0$ and $v_\varphi \simeq \sqrt{\mu_\odot/r}$ along the whole transfer. Moreover, the optimal thrust angle α^* oscillates around a mean value equal to $\text{sign}(r_f/r_0 - 1) \arctan(1/\sqrt{2})$ rad, the modulus of which is the thrust angle corresponding to the maximum transverse acceleration supplied by a conventional solar sail without attitude constraints.

The same properties are also found when dealing with circle-to-circle optimal transfer trajectories involving an SFH. This is for example confirmed by Figs. 17(a)-18(a), which show that, actually, $|\alpha^*|$ nearly coincides with 24.24 deg. The approximate expression of the minimum flight time may be obtained by



(a) Earth-Mars transfer.



(b) Earth-Venus transfer.

Figure 16: Minimum flight time as a function of a_c in a circle-to-circle interplanetary transfer.

introducing the following simplifications in Eqs. (32)–(35)

$$v_\varphi \simeq \sqrt{\frac{\mu_\odot}{r}} \quad , \quad \alpha^* = \pm \arctan\left(\frac{\sqrt{2}}{\pi}\right) \quad (43)$$

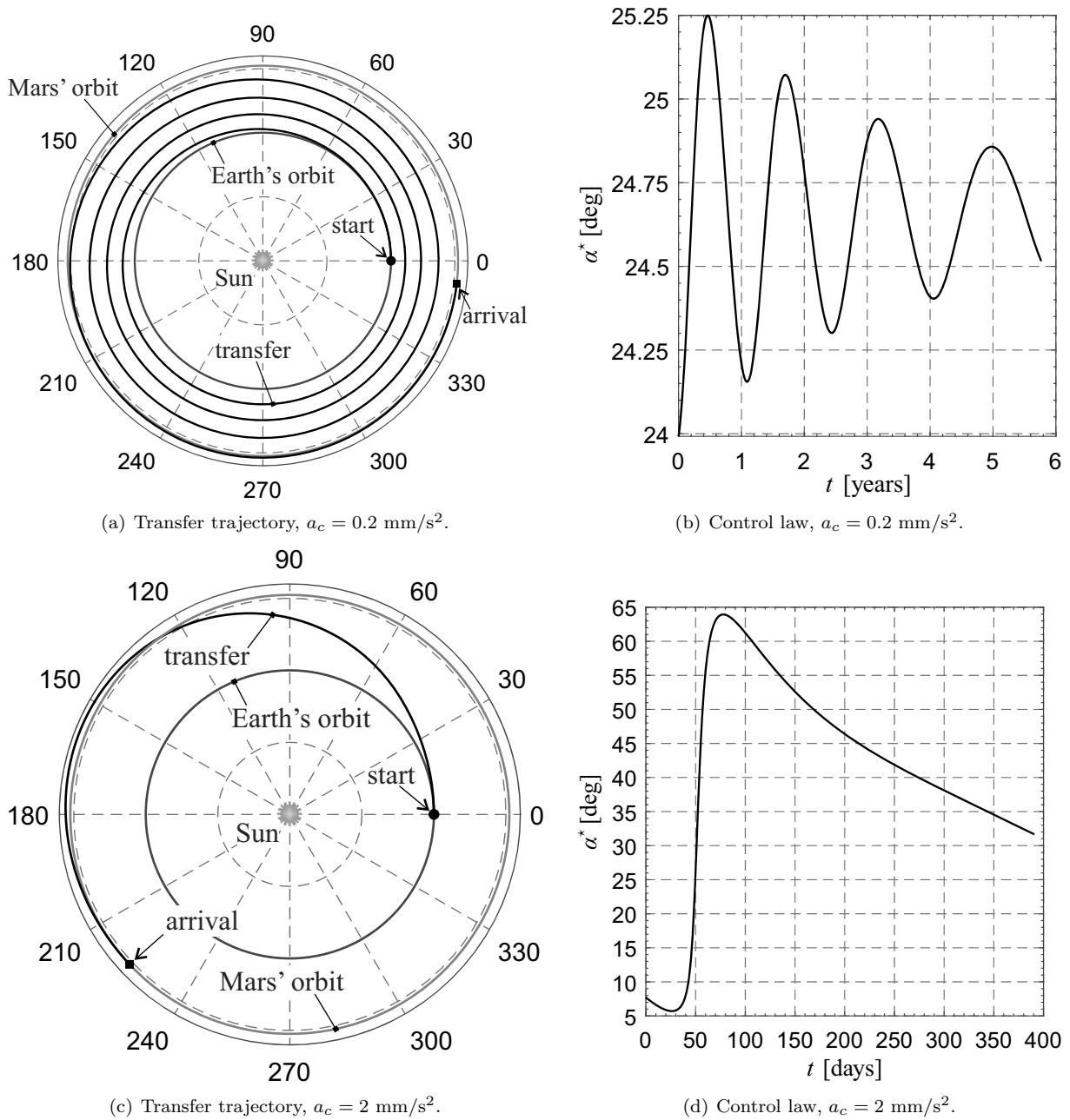


Figure 17: Earth-Mars circle-to-circle transfer with $a_c = \{0.2, 2\} \text{ mm/s}^2$.

where $\alpha^* > 0$ when $r_f/r_\oplus > 1$ (orbit raising), while $\alpha^* < 0$ when $r_f/r_\oplus < 1$ (orbit lowering). The result is

$$t_f \simeq \frac{\sqrt{3} \mu_\odot}{8 r_\oplus^2 a_c} |T_\oplus - T_f| \quad (44)$$

where T_\oplus and T_f are the orbital periods of the parking and target orbit, respectively.

The range of a_c within which Eq. (44) is valid can be determined with the aid of Fig. 19, which shows that the function $a_c t_f / (a_\oplus T_\oplus)$ (with $a_\oplus \triangleq \mu_\odot / r_\oplus^2$) is nearly constant with a_c as long as $n > 5$. An analytical expression of a_c , below which Eq. (44) gives a reasonable estimate of the total flight time, can be obtained starting from the total sweep angle $\Delta\varphi$. In fact, as previously stated, the analytical approximation given by

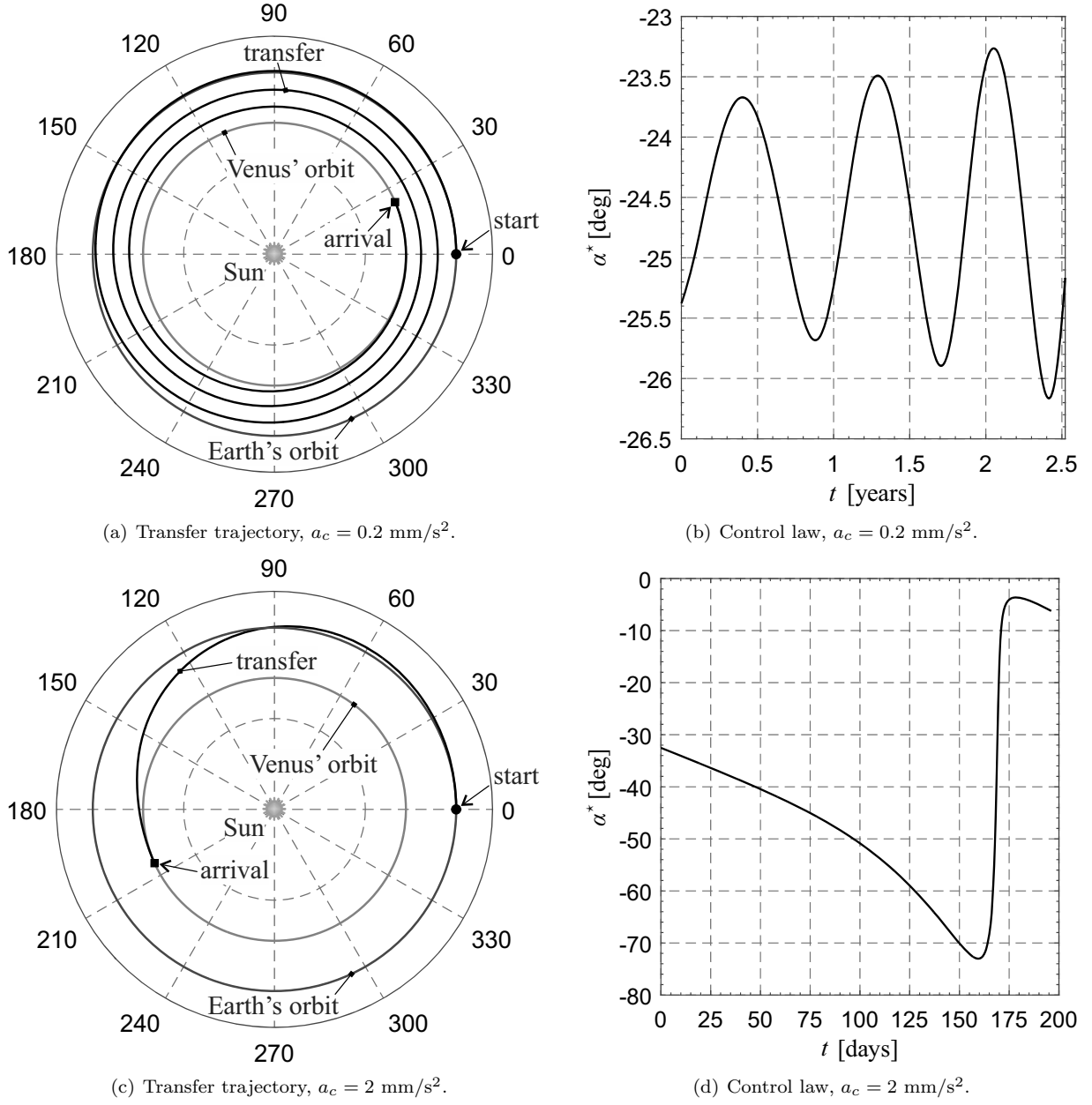


Figure 18: Earth-Venus circle-to-circle transfer with $a_c = \{0.2, 2\} \text{ mm/s}^2$.

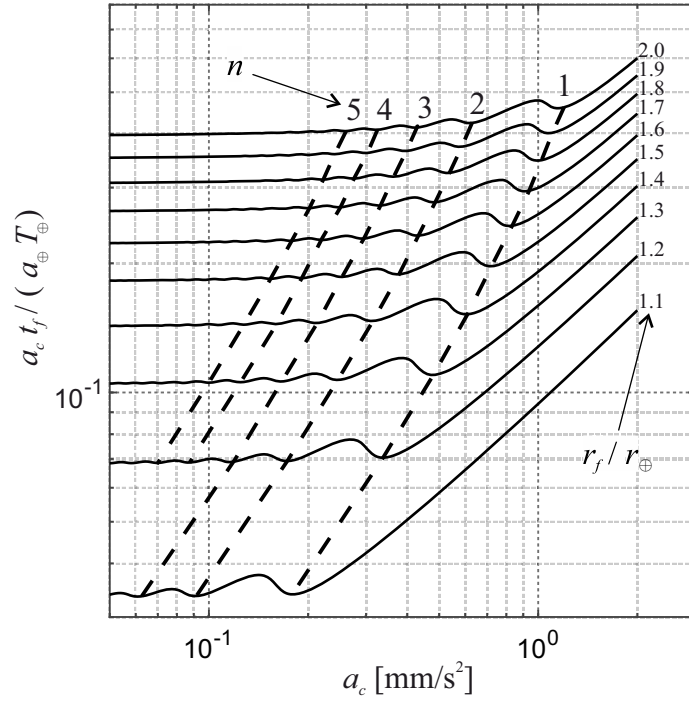
Eq. (44) is valid as long as $n > 5$, that is, when $\Delta\varphi \equiv 2\pi n > 10\pi \text{ rad}$. The total sweep angle can be found from Eqs. (33), (43), and (44), from which

$$d\varphi \simeq \frac{dt}{\sqrt{\frac{r_{\oplus}^3}{\mu_{\odot}} + \text{sign}\left(\frac{r_f}{r_{\oplus}} - 1\right) \frac{4a_c t}{\sqrt{3}\pi a_{\oplus}}}} \quad (45)$$

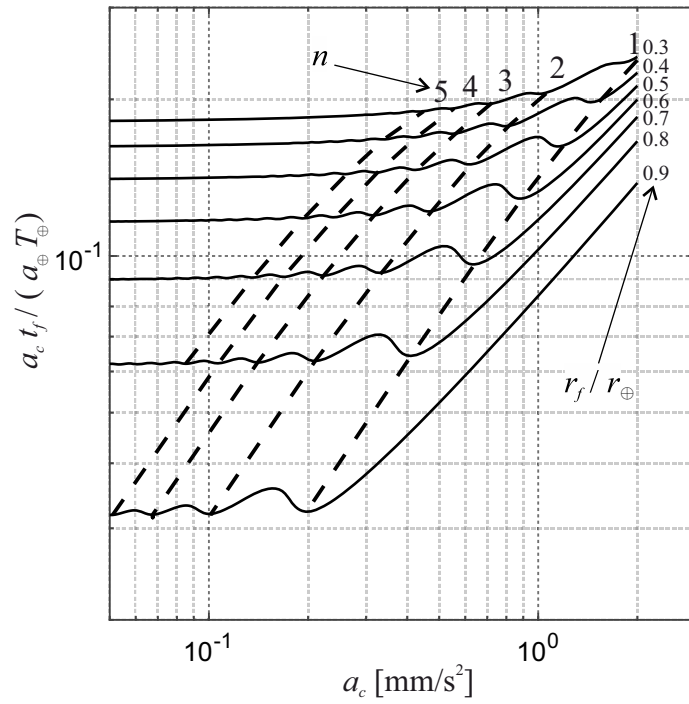
and the result of the integration is

$$\Delta\varphi \simeq \frac{3\sqrt{3}\pi a_{\oplus}}{8a_c} \left| \ln\left(\frac{r_f}{r_{\oplus}}\right) \right| \quad (46)$$

Substituting $\Delta\varphi = 10\pi \text{ rad}$ into Eq. (46), we get the maximum value of a_c below which Eq. (44) gives a



(a) Orbit raising.



(b) Orbit lowering.

Figure 19: Transfer charts for a circle-to-circle orbit transfer using an SFH.

good approximation, viz.

$$a_c < \frac{3\sqrt{3}a_\oplus}{80} \left| \ln \left(\frac{r_f}{r_\oplus} \right) \right| \quad (47)$$

Using this inequality, it is found that $a_c < 0.16 \text{ mm/s}^2$ when $r_f = 1.523 \text{ au}$ and $a_c < 0.12 \text{ mm/s}^2$ if $r_f = 0.723 \text{ au}$.

5.3. Simplified rendezvous with asteroid 25143 Itokawa

This section investigates the performance of a low-performance SFH when the target orbit is highly elliptical. As an example, consider a heliocentric transfer towards the asteroid 25143 Itokawa, that is, a potentially hazardous asteroid of the Apollo group, which has already been explored by the Japanese probe Hayabusa in 2005 [55, 56, 57]. Itokawa's heliocentric orbit has a semimajor axis $a_f = 1.3241 \text{ au}$, an eccentricity $e_f = 0.2801$ (i.e., $p_f \triangleq a_f(1 - e_f^2) \simeq 1.2202 \text{ au}$), and an orbital inclination $i_f = 1.6214 \text{ deg}$. Due to the small value of i_f , minimum-time transfer trajectories can be preliminarily investigated considering a two-dimensional mission scenario.

The minimum flight time and the corresponding number n of revolutions around the Sun for an orbit-to-orbit transfer (without ephemeris constraints) is shown in Fig. 20 as a function of a_c . In this scenario, when the value of ν_f is constrained, the minimum flight times are greater than or equal to those reported in the figure. For example, consider an SFH with $a_c = 1 \text{ mm/s}^2$. In this case, the optimal orbit-to-orbit transfer requires the rendezvous to take place when the asteroid true anomaly is $\nu_f \simeq 120 \text{ deg}$, as is shown in Fig. 21, which illustrates the transfer trajectory and the time variation of the optimal thrust angle α^* . When, instead, ν_f is constrained, the minimum flight time changes with ν_f as reported in Fig. 22.

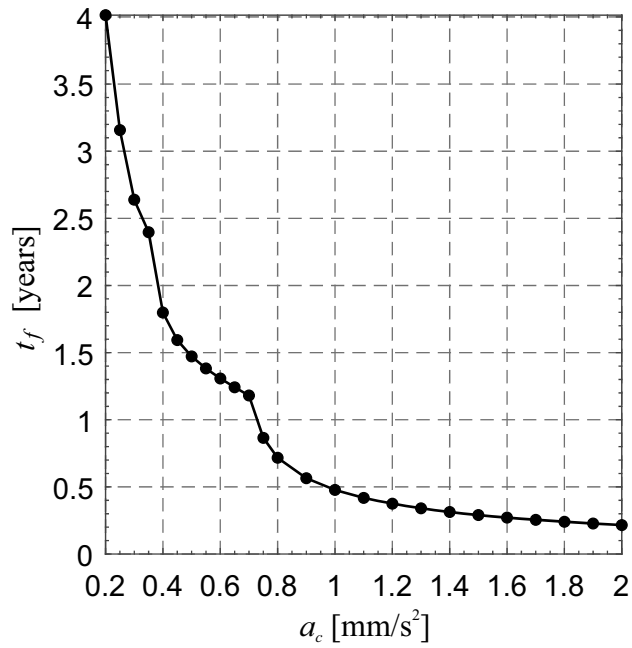
6. Conclusions

This paper has discussed a simplified analytical model for describing the propulsive acceleration vector provided by a Sun-facing heliogyro, a special configuration that occurs when the spin axis is aligned with the Sun-spacecraft line. In particular, an expression of the propulsive acceleration vector has been obtained by considering its mean value during a rotation period of the heliogyro about its spin axis. In this regard, the mean transverse propulsive acceleration provided by a Sun-facing heliogyro is reduced by a factor $(1 - 2/\pi)$ when compared to that given by a conventional solar sail without attitude constraints. As expected, the torque that arises from the generation of the propulsive acceleration is (at least on average) equal to zero. The thrust model has been used for analytically determining the optimal steering law, which has been applied to solve a set of minimum-time rendezvous problems between coplanar heliocentric orbits. Some exemplary cases, including transfers to the asteroid 25143 Itokawa, to Mars and to Venus have been studied as a function of the heliogyro characteristic acceleration.

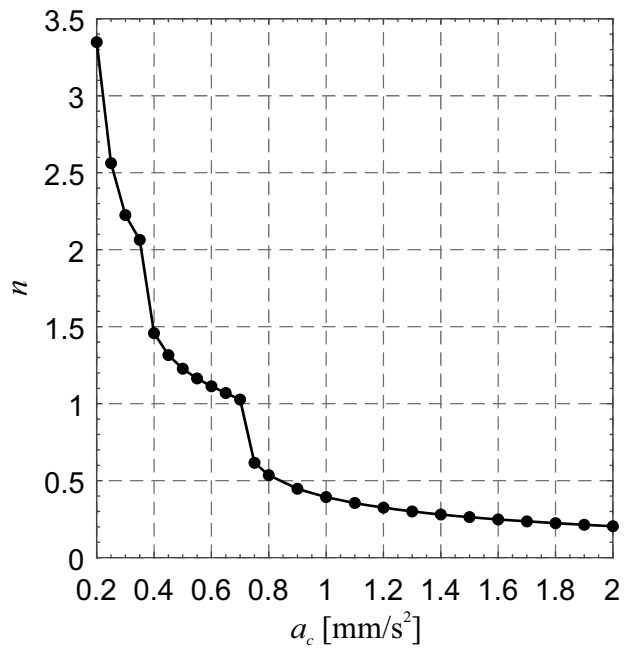
A natural extension of this work is to include the optical characteristics of the reflective film in the description of the heliogyro thrust and the torque vectors. In addition, a more detailed performance analysis of a heliogyro-based spacecraft in a three-dimensional mission scenario should also consider the spacecraft mass budget model, in order to estimate the actual value of the characteristic acceleration as a function of the reflective surface area and the payload mass. Finally, the performance of a Sun-facing heliogyro could also be analyzed in a more challenging planetary escape/capture scenario, where the high orbit rates could make the thrust orientation more difficult to obtain. In fact, during a planetary escape/capture phase, the orbit rate is typically so high that the heliogyro may not be able to rotate its fundamental plane fast enough. In that case, a Sun-facing cyclic thrust profile may represent the only possible control strategy.

Conflict of interest statement

The authors declared that they have no conflicts of interest to this work.



(a) Total flight time.



(b) Number of revolutions.

Figure 20: Minimum flight time and corresponding number of revolutions around the Sun as a function of a_c for an Earth-25143 Itokawa transfer.

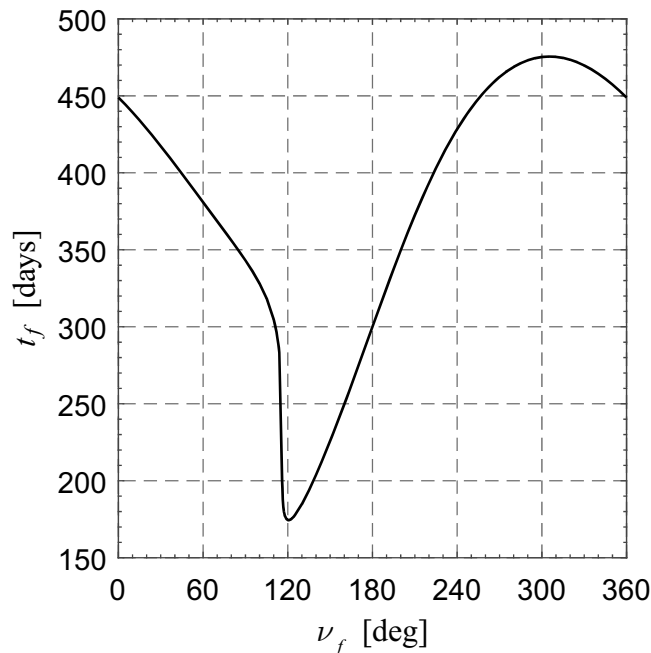


Figure 22: Minimum flight time as a function of ν_f for an Earth-25143 Itokawa transfer with $a_c = 1 \text{ mm/s}^2$.

References

- [1] C. R. McInnes, *Solar Sailing: Technology, Dynamics and Mission Applications*, Springer-Praxis Series in Space Science and Technology, Springer-Verlag, Berlin, 1999.
- [2] S. Gong, M. Macdonald, Review on solar sail technology, *Astrodynamics* 3 (2) (2019) 93–125, doi: 10.1007/s42064-019-0038-x.
- [3] D. A. Spencer, L. Johnson, A. C. Long, Solar sailing technology challenges, *Aerospace Science and Technology* 93 (2019) Article number 105276, doi: 10.1016/j.ast.2019.07.009.
- [4] X. Hu, S. Gong, Flexibility influence on passive stability of a spinning solar sail, *Aerospace Science and Technology* 58 (2016) 60–70, doi: 10.1016/j.ast.2016.08.005.
- [5] B. Fu, F. Eke, Further investigation of the body torques on a square solar sail due to the displacement of the sail attachment points, *Aerospace Science and Technology* 50 (2016) 281–294, doi: 10.1016/j.ast.2016.01.007.
- [6] B. Fu, R. T. Farouki, F. O. Eke, Equilibrium configuration of a bounded inextensible membrane subject to solar radiation pressure, *Aerospace Science and Technology* 68 (2017) 552–560, doi: 10.1016/j.ast.2017.06.018.
- [7] X. Pan, M. Xu, R. Santos, Trajectory optimization for solar sail in cislunar navigation constellation with minimal lightness number, *Aerospace Science and Technology* 70 (2017) 559–567, doi: 10.1016/j.ast.2017.08.042.
- [8] Y. Song, S. Gong, Solar-sail trajectory design for multiple near-earth asteroid exploration based on deep neural networks, *Aerospace Science and Technology* 91 (2019) 28–40, doi: 10.1016/j.ast.2019.04.056.
- [9] S. Firuzi, S. Gong, Refractive sail and its applications in solar sailing, *Aerospace Science and Technology* 77 (2018) 362–372, doi: 10.1016/j.ast.2018.03.016.
- [10] M. Bassetto, A. Caruso, A. A. Quarta, G. Mengali, Optimal steering law of refractive sail, *Advances in Space Research* 67 (9) (2021) 2855–2864, doi: 10.1016/j.asr.2019.10.033.
- [11] W. Wang, H. Baoyin, G. Mengali, A. A. Quarta, Solar sail cooperative formation flying around L_2 -type artificial equilibrium points, *Acta Astronautica* 169 (2020) 224–239, doi: 10.1016/j.actaastro.2019.10.028.
- [12] A. Piloni, A. V. Rao, M. Ceriotti, Automated Trajectory Optimizer for Solar Sailing (ATOSS), *Aerospace Science and Technology* 72 (2018) 465–475, doi: 10.1016/j.ast.2017.11.025.
- [13] J. Sauer, C. G., Optimum solar-sail interplanetary trajectories, in: *AIAA/AAS Astrodynamics Conference*, San Diego (CA), August 18–20, 1976, paper AIAA 76-792. doi: 10.2514/6.1976-792.
- [14] G. Mengali, A. A. Quarta, Optimal three-dimensional interplanetary rendezvous using non-ideal solar sail, *Journal of Guidance, Control, and Dynamics* 28 (1) (2005) 173–177, doi: 10.2514/1.8325.
- [15] L. Niccolai, A. A. Quarta, G. Mengali, Analytical solution of the optimal steering law for non-ideal solar sail, *Aerospace Science and Technology* 62 (2017) 11–18, doi: 10.1016/j.ast.2016.11.031.
- [16] R. H. MacNeal, The heliogyro, an interplanetary flying machine, Contractor Report (CR) NASA-CR-84460, NASA, available online (cited November 15, 2020) <https://ntrs.nasa.gov/api/citations/19670018298/downloads/19670018298.pdf> (Mar. 1967).
- [17] R. H. MacNeal, J. M. Hedgepeth, H. U. Schuerch, Heliogyro solar sailer summary report, Contractor Report (CR) NASA-

- CR-1329, NASA, available online (cited November 15, 2020) <https://ntrs.nasa.gov/api/citations/19690019483/downloads/19690019483.pdf> (Jun. 1969).
- [18] R. H. MacNeal, Structural dynamics of the heliogyro, Contractor Report (CR) NASA-CR-1745, NASA, available online (cited November 15, 2020) <https://ntrs.nasa.gov/api/citations/19710018523/downloads/19710018523.pdf> (May 1971).
- [19] R. H. MacNeal, Heliogyro preliminary design, phase II final report, Contractor Report (CR) NASA-CR-157128, NASA, available online (cited November 15, 2020) <https://ntrs.nasa.gov/api/citations/19780016313/downloads/19780016313.pdf> (Jan. 1978).
- [20] R. H. MacNeal, J. M. Hedgepeth, Helicopters for interplanetary space flight, in: 34th National Forum of the American Helicopter Society, Washington D.C., may, 1978.
- [21] J. L. Wright, Space Sailing, Gordon and Breach Science Publishers, 1992, pp. 223–233.
- [22] M. MacDonald (Ed.), Advances in Solar Sailing, Springer-Verlag Berlin Heidelberg, 2014, pp. 631–830.
- [23] W. K. Wilkie, J. E. Warren, L. G. Horta, K. H. Lyle, J. Juang, J. D. Littell, R. G. Bryant, M. W. Thomson, P. E. Walkemeyer, D. V. Guerrant, D. A. Lawrence, S. C. Gibbs, E. H. Dowell, A. F. Heaton, Heliogyro solar sail research at NASA, in: Proceedings of the Third International Symposium on Solar Sailing, Glasgow (UK), June 11–13, 2013.
- [24] J.-N. Juang, H.-H. Lu, L. G. Horta, W. K. Wilkie, Dynamics of a coupled pendulum model of a heliogyro membrane blade, in: Proceedings of the Third International Symposium on Solar Sailing, Glasgow (UK), June 11–13, 2013.
- [25] J. N. Juang, H. H. Lu, L. G. Horta, K. W. Wilkie, Challenges associated with system identification and control of a heliogyro membrane blade, in: Proceedings of the Third International Symposium on Solar Sailing, Glasgow (UK), June 11–13, 2013.
- [26] C. S. Gibbs, E. H. Dowell, Solarelastic stability of the heliogyro, in: Proceedings of the Third International Symposium on Solar Sailing, Glasgow (UK), June 11–13, 2013.
- [27] D. Guerrant, D. Lawrence, Heliogyro attitude control moment authority via blade pitch maneuvers, in: Proceedings of the Third International Symposium on Solar Sailing, Glasgow (UK), June 11–13, 2013.
- [28] D. V. Guerrant, W. K. Wilkie, D. A. Lawrence, Heliogyro blade twist control via reflectivity modulation, in: 53rd AIAA/ASME/ASCE/AHS/ASC Structures, Structural Dynamics and Materials Conference, Honolulu, Hawaii, 23–26 April, 2012, paper AIAA 2012-1746. doi: 10.2514/6.2012-1746.
- [29] D. V. Guerrant, D. A. Lawrence, Heliogyro solar sail blade twist stability analysis of root and reflectivity controllers, in: AIAA Guidance, Navigation, and Control Conference, Minneapolis, Minnesota, 13–16 August, 2012, paper AIAA 2012-4842. doi: 10.2514/6.2012-4842.
- [30] D. V. Guerrant, D. A. Lawrence, W. K. Wilkie, Performance of a heliogyro blade twist controller with finite bandwidth, in: AIAA/AAS Astrodynamics Specialist Conference, Minneapolis, Minnesota, 13–16 August, 2012, paper AIAA 2012-4661. doi: 10.2514/6.2012-4661.
- [31] D. V. Guerrant, D. A. Lawrence, W. K. Wilkie, Dynamics and control of the helios solar sail demonstrator, in: Proceedings of the International Astronautical Congress (IAC), Naples, Italy, 1–5 October, 2012.
- [32] D. V. Guerrant, D. A. Lawrence, Nonlinear torsional dynamics and control of heliogyro solar sail blades, in: 2nd AIAA Spacecraft Structures Conference, Kissimmee (FL), 5–9 January, 2015, paper AIAA 2015-0435. doi: 10.2514/6.2015-0435.
- [33] D. V. Guerrant, D. A. Lawrence, Tactics for heliogyro solar sail attitude control via blade pitching, *Journal of Guidance, Control, and Dynamics* 38 (9) (2015) 1785–1799, doi: 10.2514/1.G000861.
- [34] W. K. Wilkie, J. E. Warren, L. G. Horta, K. H. Lyle, J.-N. Juang, S. C. Gibbs, E. H. Dowell, D. V. Guerrant, D. A. Lawrence, Recent advances in heliogyro solar sail structural dynamics, stability, and control research, in: 2nd AIAA Spacecraft Structures Conference, Kissimmee (FL), 5–9 January, 2015, paper AIAA 2015-0431. doi: 10.2514/6.2015-0431.
- [35] J. Heiligers, D. V. Guerrant, D. A. Lawrence, Solving the heliogyro’s inverse problem, in: AIAA/AAS Astrodynamics Specialist Conference, Long Beach (CA), 13–16 September, 2016, paper AIAA 2016-5334. doi: 10.2514/6.2016-5334.
- [36] J. Heiligers, D. V. Guerrant, D. A. Lawrence, Exploring the heliogyro’s orbital control capabilities for solar sail halo orbits, *Journal of Guidance, Control, and Dynamics* 40 (10) (2017) 2569–2586, doi: 10.2514/1.G002184.
- [37] A. Pimienta-Peñalver, L. Tsai, J.-N. Juang, J. L. Crassidis, System modeling and control of a heliogyro solar sail, in: AIAA Guidance, Navigation, and Control Conference, Kissimmee (FL), 8–12 January, 2018, paper AIAA 2018-1311. doi: 10.2514/6.2018-1311.
- [38] A. Pimienta-Peñalver, L.-W. Tsai, J.-N. Juang, J. L. Crassidis, Heliogyro solar sail structural dynamics and stability, *Journal of Guidance, Control, and Dynamics* 42 (8) (2019) 1645–1657, doi: 10.2514/1.G003758.
- [39] G. W. Kim, S. B. Choi, J. Kang, Dynamic modeling and spin control for deployment of spin-type heliogyro solar sail, *Journal of Spacecraft and Rockets* 57 (3) (2020) 464–472, doi: 10.2514/1.A34582.
- [40] J.-N. Juang, J. E. Warren, L. G. Horta, W. K. Wilkie, A multi-blade model for heliogyro solar sail structural dynamic analysis, *Journal of the Astronautical Sciences* 67 (2) (2020) 335–360, doi: 10.1007/s40295-019-00153-8.
- [41] J. Kang, K.-C. Park, Solarelastic instability of periodically time-varying heliogyro blade, *Journal of Spacecraft and Rockets* 57 (2) (2020) 398–404, doi: 10.2514/1.A34563.
- [42] J. Kang, K.-C. Park, Flexible heliogyro solar sail under solar radiation pressure and gravitational force, *Acta Astronautica* 79 (2021) 186–196, doi: 10.1016/j.actaastro.2020.10.042.
- [43] S. M. Cook, D. A. Lawrence, J. E. Warren, W. K. Wilkie, Improved modal damping characterization for small-scale heliogyro blades, *Journal of Spacecraft and Rockets* 57 (4) (2020) 642–655, doi: 10.2514/1.A34518.
- [44] S. M. Cook, D. A. Lawrence, Sensitivity of a physically realizable heliogyro root pitch control system to inherent damping models, *Advances in Space Research*, 67 (9) (2021) 2696–2705, doi: 10.1016/j.asr.2020.09.008.
- [45] D. V. Guerrant, Performance quantification of heliogyro solar sails using structural, attitude, and orbital dynamics and control analysis, Ph.D. thesis, University of Colorado Boulder, Boulder, CO, available online (cited March 07, 2021): <https://scholar.colorado.edu/downloads/3x816m84q> (2015).
- [46] R. Blomquist, Heliogyro control, Ph.D. thesis, Carnegie Mellon University, Pittsburgh, PA, available online (cited November 15, 2020) https://ri.cmu.edu/pub_files/2009/4/DissertationLatex.pdf (April 2009).

- [47] A. Caruso, L. Niccolai, A. A. Quarta, G. Mengali, Effects of attitude constraints on solar sail optimal interplanetary trajectories, *Acta Astronautica* 177 (2020) 39–47, doi: 10.1016/j.actaastro.2020.07.010.
- [48] B. Dachwald, et al., Potential solar sail degradation effects on trajectory and attitude control, in: *AIAA Guidance, Navigation, and Control Conference and Exhibit*, San Francisco, USA, 2005, paper AIAA 2005-6172.
- [49] B. Dachwald, G. Mengali, A. A. Quarta, M. Macdonald, Parametric model and optimal control of solar sails with optical degradation, *Journal of Guidance, Control, and Dynamics* 29 (5) (2006) 1170–1178, doi: 10.2514/1.20313.
- [50] B. Dachwald, M. Macdonald, C. R. McInnes, G. Mengali, A. A. Quarta, Impact of optical degradation on solar sail mission performance, *Journal of Spacecraft and Rockets* 44 (4) (2007) 740–749, doi: 10.2514/1.21432.
- [51] G. Mengali, A. A. Quarta, C. Circi, B. Dachwald, Refined solar sail force model with mission application, *Journal of Guidance, Control, and Dynamics* 30 (2) (2007) 512–520, doi: 10.2514/1.24779.
- [52] G. Mengali, A. A. Quarta, Optimal heliostationary missions of high-performance sailcraft, *Acta Astronautica* 60 (8-9) (2007) 676–683, doi: 10.1016/j.actaastro.2006.07.018.
- [53] D. F. Lawden, *Optimal Trajectories for Space Navigation*, Butterworths & Co., London, 1963, pp. 54–60.
- [54] A. A. Quarta, G. Mengali, Semi-analytical method for the analysis of solar sail heliocentric orbit raising, *Journal of Guidance, Control, and Dynamics* 35 (1) (2012) 330–335, doi: 10.2514/1.55101.
- [55] S. C. Lowry, P. R. Weissman, M. D. Hicks, R. J. Whiteley, S. Larson, Physical properties of asteroid (25143) Itokawa - Target of the Hayabusa sample return mission, *Icarus* 176 (2) (2005) 408–417, doi: 10.1016/j.icarus.2005.02.002.
- [56] T. G. Müller, T. Sekiguchi, M. Kaasalainen, M. Abe, S. Hasegawa, Thermal infrared observations of the Hayabusa spacecraft target asteroid 25143 Itokawa, *Astronomy and Astrophysics* 443 (1) (2005) 347–355, doi: 10.1051/0004-6361:20053862.
- [57] M. Abe, Y. Takagi, K. Kitazato, S. Abe, T. Hiroi, F. Vilas, B. E. Clark, P. A. Abell, S. M. Lederer, K. S. Jarvis, T. Nimura, Y. Ueda, A. Fujiwara, Near-infrared spectral results of asteroid Itokawa from the Hayabusa spacecraft, *Science* 312 (5778) (2006) 1334–1338, doi: 10.1126/science.1125718.